Journal of Applied Physics

Micromagnetic Monte Carlo method with variable magnetization length based on the Landau–Lifshitz–Bloch equation for computation of large-scale thermodynamic equilibrium states

Cite as: J. Appl. Phys. **130**, 163902 (2021); https://doi.org/10.1063/5.0059745
Submitted: 11 June 2021 • Accepted: 20 September 2021 • Published Online: 26 October 2021

Serban Lepadatu

Journal of Applied Physics METHOD scitation.org/journal/jap

Micromagnetic Monte Carlo method with variable magnetization length based on the Landau–Lifshitz–Bloch equation for computation of large-scale thermodynamic equilibrium states

Cite as: J. Appl. Phys. **130**, 163902 (2021); doi: 10.1063/5.0059745
Submitted: 11 June 2021 · Accepted: 20 September 2021 ·
Published Online: 26 October 2021

Serban Lepadatu[a)]

AFFILIATIONS

Jeremiah Horrocks Institute for Mathematics, Physics and Astronomy, University of Central Lancashire, Preston PR1 2HE, United Kingdom

[a)]**Author to whom correspondence should be addressed:** SLepadatu@uclan.ac.uk

ABSTRACT

An efficient method for computing thermodynamic equilibrium states at the micromagnetic length scale is introduced using the Markov chain Monte Carlo method. Trial moves include not only rotations of vectors, but also a change in their magnetization length. The method is parameterized using the longitudinal susceptibility, reproduces the same Maxwell–Boltzmann distribution as the stochastic Landau–Lifshitz–Bloch equation, and is applicable both below and above the Curie temperature. The algorithm is fully parallel, can be executed on graphical processing units, and efficiently includes the long-range dipolar interaction. This method is generally useful for computing finite-temperature relaxation states for both uniform and non-uniform temperature profiles and can be considered as complementary to zero-temperature micromagnetic energy minimization solvers, with comparable computation time. Compared to the dynamic approach, it is shown that the micromagnetic Monte Carlo method is up to almost 20 times faster. Moreover, unlike quasizero temperature approaches that do not take into account the magnetization length distribution and stochasticity, the method is better suited for structures with unbroken symmetry around the applied field axis, granular films, and at higher temperatures and fields. In particular, applications to finite-temperature hysteresis loop modelling, chiral magnetic thin films, granular magnetic media, and artificial spin ices are discussed.

I. INTRODUCTION

Monte Carlo computations are widely used in many fields of research, including statistical physics and atomistic spin lattice modelling. For the Ising and Heisenberg Hamiltonian spin lattice models, the Metropolis Monte Carlo[1] algorithm has proved popular. This allows computation not only of magnetic parameters temperature dependences and phase transition temperatures, but also of hysteresis loops.[2] In micromagnetics modelling, a common need is computation of relaxed magnetization states. For zero-temperature models, this may be accomplished efficiently using energy minimization solvers, such as a steepest descent method.[3] Finite-temperature micromagnetic models include the stochastic Landau–Lifshitz–Gilbert equation (sLLG)[4] and the Landau–Lifshitz–Bloch (LLB) equation[5] and its stochastic forms (sLLB).[6,7] Although the sLLG equation is a reasonable approximation at low temperatures, it fails to take into account the magnetization length distribution, which has been shown to play an important role in magnetization reversal,[8] including linear and elliptical reversal mechanisms,[9] particularly for temperatures approaching the Curie point. Thus, while the sLLB equation may be used to compute finite-temperature relaxation states, this dynamic approach to relaxation is very inefficient and requires lengthy computation times. Alternative methods, such as a Monte Carlo approach, are required to efficiently compute relaxation states of thermodynamic equilibrium, which should ideally be applicable across the entire temperature range, both below and above the Curie temperature; for this reason, correct reproduction of the magnetization length probability distribution at the micromagnetic length scale is essential.

A previous work extended the Monte Carlo method to the micromagnetic length scale; however, the magnetization length

distribution was not taken into account;[10] the resulting thermodynamic equilibrium properties are the same as those produced by the sLLG equation. Other works along this line also include a micromagnetic one-dimensional model[11] and a two-dimensional model.[12] Alternatively, a thermodynamic rescaling for the atomistic cluster Monte Carlo approach was also discussed.[13] A Monte Carlo method was also used for the Landau–Heisenberg Hamiltonian, applied to the study of phase transitions in FeRh including magnetic and non-magnetic contributions.[14] A micromagnetic hybrid Monte Carlo method was introduced previously[15] based on the hybrid (molecular dynamics/Langevin) Monte Carlo approach,[16] which reproduces a Boltzmann distribution for free energy. At the micromagnetic length scale however, particularly when approaching the Curie temperature, the distribution of the free energy does not follow a Boltzmann distribution but a Maxwell–Boltzmann type distribution.[7] Moreover, for the purposes of computing thermodynamic equilibrium states at the micromagnetic length scale, the hybrid Monte Carlo approach is inefficient, since an ensemble of conjugate momenta must be evolved over many iterations (typically 100 or more), before a new micromagnetic magnetization configuration may be accepted or rejected.

Here we describe a micromagnetic Monte Carlo (MMC) method based on the Markov Chain approach, thus similar to the Metropolis Monte Carlo method[1] commonly used for atomistic spin lattice simulations but including trial moves for magnetization length change. The resulting method not only correctly reproduces the expected Maxwell–Boltzmann distribution for the free energy but generates new micromagnetic magnetization configurations for every iteration. The algorithm has been implemented in Boris[17] and is publically available and open-source.[18] In Sec. II, the algorithm and related theory are described and tested. In Sec. III, the inclusion of the long-range demagnetizing interaction in the parallel MMC implementation is described and tested by the computation of hysteresis loops and comparison with established methods. In Sec. IV, the application of MMC to chiral magnetic films with Dzyaloshinsky–Moriya interaction (DMI)[19,20] is discussed. Finally, in Sec. V, the application of MMC to the study of artificial spin ices (ASI) is addressed, before summarizing possible future developments in the concluding remarks.

II. MICROMAGNETIC MARKOV CHAIN MONTE CARLO METHOD

For atomistic spin lattice models, where the spins have fixed length, at thermodynamic equilibrium, the internal energy E follows a Boltzmann distribution, $\exp(-E/k_BT)/Z$, where Z is the partition function, k_B is the Boltzmann constant, and T is the temperature. At the micromagnetic length scale however, where the magnetization length can vary due to thermodynamic averaging over many atomistic spins, the distribution of the free energy follows a Maxwell–Boltzmann type distribution,[7] given as follows:

$$f(\mathbf{m}) = m^2\exp(-F(\mathbf{m})/k_BT)/Z,$$
$$Z = \sum_i m_i^2\exp(-F(\mathbf{m}_i)/k_BT). \tag{1}$$

Here, $\mathbf{m} = \mathbf{M}/M_{S0}$, where $\mathbf{M}$ is the magnetization vector and M_{S0} is the zero-temperature saturation magnetization, and $m = |\mathbf{m}|$. $F(\mathbf{m})$ is the micromagnetic free energy and contains a number of interactions, including applied field, exchange interaction, DMI, magnetocrystalline anisotropy, and demagnetizing interaction. The distribution in Eq. (1) is reproduced by the sLLB equation[7] and atomistic spin lattice simulations where the magnetization is computed by thermodynamic averaging of atomistic spins, as we have verified numerically. While the sLLB equation may be used to compute relaxed magnetization states in thermodynamic equilibrium, as required, for example, for finite-temperature hysteresis loop modelling, this approach is very inefficient, particularly for large-scale simulations. A far more efficient approach may be obtained using a Monte Carlo method. In particular, we wish to establish a method that generates the distribution in Eq. (1), using a similar method to the Metropolis Monte Carlo[1] employed for atomistic spin lattices, by generating new micromagnetic magnetization configurations every iteration. For atomistic simulations, trial moves generally consist of spin rotations about the initial direction. For micromagnetic simulations, where the magnetization length is not fixed, we must compound this by an additional trial move, namely, a change in the magnetization length. A Monte Carlo iteration then consists of a sequence of trial moves, exactly one per micromagnetic magnetization vector (rotation and length change), each of which is accepted with a given probability. In the Markov chain Monte Carlo approach, a sequence of ensembles is generated, which converges to the required thermodynamic equilibrium distribution. A sufficient condition for convergence is that of detailed balance,

$$f(\mathbf{m}_A)W(A \to B) = f(\mathbf{m}_B)W(B \to A). \tag{2}$$

Here, $W(A \to B)$ is the transition probability from state A to state B in the Markov chain. Thus, we obtain the following ratio:

$$\frac{W(A \to B)}{W(B \to A)} = \frac{m_B^2}{m_A^2}\exp(-\Delta F/k_BT),$$
$$\Delta F = F(\mathbf{m}_B) - F(\mathbf{m}_A). \tag{3}$$

The Markov chain transition probability is given by

$$W(A \to B) = p(A)P_{\text{accept}}(A \to B),$$
$$p(A) \propto m_A^2. \tag{4}$$

Here, $P_{\text{accept}}(A \to B)$ is the trial move acceptance probability, and $p(A)$ is the conditional probability. For atomistic spin lattice simulations, we simply have $p(A) = 1/N$, where N is the total number of spins, i.e., each spin receives an equal weight. For micromagnetic magnetization vectors however, the weight is proportional to m^2, as may be seen by inspecting the partition function in Eq. (1). Thus, we arrive at the following acceptance probability that satisfies Eq. (3) and hence the detailed balance:

$$P_{\text{accept}}(A \to B) = \min\left\{1, \frac{m_B^4}{m_A^4}\exp(-\Delta F/k_BT)\right\}. \tag{5}$$

In Eq. (1), we now separate the longitudinal energy contribution and rewrite it as

$$f(\mathbf{m}) = \exp(-F(\hat{\mathbf{m}})/k_B T) f_l(m) Z_l / Z. \tag{6}$$

Here, $f_l(m)$ is the magnetization length probability distribution, with Z_l being a renormalization factor, given by

$$f_l(m) = \frac{m^2}{Z_l} \begin{cases} \exp\left(-\dfrac{VM_{S0}}{8\tilde{\chi}_{||} m_e^2 k_B T}(m^2 - m_e^2)^2\right), & T < T_C \\ \exp\left(-\dfrac{VM_{S0}m^2}{2\tilde{\chi}_{||} k_B T}\left(1 + \dfrac{3T_C m^2}{10(T - T_C)}\right)\right), & T > T_C. \end{cases} \tag{7}$$

The longitudinal term contribution in Eq. (7), where V is the micromagnetic computational cell size volume (e.g., $V = h^3$ for a cubic cell with cell size h), is the same which appears in the sLLB or LLB equation and which gives rise to a longitudinal field. It is parametrized using the relative longitudinal susceptibility given as[5]

$$\tilde{\chi}_{||}(T) = \frac{\mu}{k_B T} \frac{B'(x)}{1 - B'(x)(3T_C/T)}, \quad x = m_e 3T_C/T. \tag{8}$$

Here, $B(x) = \coth(x) - 1/x$ is the Langevin function, μ is the atomic moment, T_C is the Curie temperature, and $m_e = M_e/M_{s0}$ is the normalized temperature-dependent equilibrium magnetization length given as[5]

$$m_e(T) = B\left[m_e \frac{3T_C}{T} + \frac{\mu\mu_0 H_{\text{ext}}}{k_B T}\right]. \tag{9}$$

The remaining terms that contribute to free energy $F(\hat{\mathbf{m}})$ in Eq. (6) include all the usual micromagnetic terms, and these may be obtained directly from the corresponding energy density terms by multiplying with the computational cell size volume V. There are a few terms that require special attention however, namely, exchange interactions (direct and DMI) and demagnetizing interaction. First we treat the direct exchange interaction and discuss the remaining terms later. The micromagnetic exchange free energy for a given magnetization vector i is given below, where A is the temperature-dependent exchange stiffness,

$$F_{\text{ex},i} = -V \frac{2A}{M_e^2} \mathbf{M}_i . \nabla^2 \mathbf{M}_i. \tag{10}$$

It is important to note the multiplicative factor of 2 here: the micromagnetic exchange energy density (see Ref. 17) expression is derived from the atomistic Heisenberg direct exchange Hamiltonian contribution that includes compensation for double-counting of spins. In order to calculate the free energy contribution of a single magnetization vector however, just as with the atomistic Monte Carlo method, the factor of 2 must be restored.

Single-site energy terms are obtained directly from the corresponding micromagnetic energy density expressions,[17] for example, the uniaxial magnetocrystalline anisotropy is included as

$$F_{\text{Uan},i} = VK_1[1 - (\mathbf{m}_i . \mathbf{e_A})^2] + VK_2[1 - (\mathbf{m}_i . \mathbf{e_A})^2]^2. \tag{11}$$

Here, $\mathbf{e_A}$ is the symmetry axis direction, and K_1 and K_2 are the second and fourth order uniaxial anisotropy constants, respectively. Cubic magnetocrystalline anisotropy is included as

$$F_{\text{Can},i} = VK_1[\alpha_i^2\beta_i^2 + \alpha_i^2\gamma_i^2 + \beta_i^2\gamma_i^2] + VK_2\alpha_i^2\beta_i^2\gamma_i^2. \tag{12}$$

Here, K_1 and K_2 are the fourth and sixth order cubic anisotropy constants, respectively, α_i, β_i, and γ_i are direction cosines of the magnetization vector.

Thus, the MMC method consists of the following steps: (1) for a vector i perform a rotation trial move in a cone of given solid angle. (2) For the same vector i perform a magnetization length change trial move. (3) Compute the total free energy change, including the longitudinal free energy change using the energy term appearing in the exponent of Eq. (7). (4) Accept the compound trial move with probability given in Eq. (5). This procedure is done exactly once for each micromagnetic vector, which completes an MMC iteration. The algorithm is fully parallel, implemented with the red–black checkerboard decomposition scheme discussed previously for the atomistic Monte Carlo algorithm,[21,22] and is thus suitable for computations on graphical processing units (GPUs). The final question is how the solid angle for the rotation trial moves should be chosen and how the magnetization length should be changed. With time-quantized Monte Carlo (TQMC),[23,24] the cone solid angle is set such that real-time processes may be reproduced, for example, the effect of the field sweep rate on hysteresis loops[25] or thermally activated grain reversal time.[26] This may also be possible with MMC; however, this topic is outside the scope of the current work. Instead, the cone solid angle is adaptively set such that the acceptance rate is kept at an optimal value of ∼0.5,[22] which allows rapid thermalization across the entire applicable temperature range.

The acceptance rate is computed every 100 iterations, and the cone angle adjusted by 1° up or down if an acceptance tolerance threshold of ±0.05 is exceeded, in order to decrease or respectively increase the acceptance rate. During thermodynamic equilibrium, this typically results in a cone angle variation around a mean value with a standard deviation of ∼1°. The magnetization length change is performed by multiplying with a random factor uniformly chosen in the range $[1 - \sigma, 1 + \sigma]$, where $0 < \sigma < 1$. At low temperatures, σ should be small in order to avoid excessive rejection of trial steps, while at high temperatures σ should be large enough to allow for rapid convergence to thermodynamic equilibrium. A good choice for σ may be obtained by noticing from Eq. (7) that $f_l(m)/m^2$ is a Gaussian distribution of m^2 with mean m_e^2 and width σ given by

$$\sigma = 2m_e \sqrt{\frac{\tilde{\chi}_{||} k_B T}{VM_{S0}}}. \tag{13}$$

In practice, this needs to be capped to a maximum value, and we use $\sigma \lesssim 0.03$ that is reached close to T_C, and also for $T > T_C$, this

latter constant value is used. It should be noted that since the algorithm generates a magnetization length distribution governed by Eq. (7), the probability of generating a vector with $|\mathbf{M}| > M_{S0}$ is practically zero.

We now verify the MMC method that correctly reproduces the target probability distribution by comparison with the sLLB equation. For this purpose, a $50 \times 50 \times 50$ nm simulation space is chosen with parameters typical for $Ni_{80}Fe_{20}$ [$M_{s0} = 800$ kA/m, $A(T) = A_0 m_e^2$[27] with $A_0 = 13$ pJ/m]; a value of $T_C = 680$ K was set. The direct exchange interaction is enabled with periodic boundary conditions in all directions, and a magnetic field of 10 kA/m is applied. The sLLB equation is implemented as given in Ref. 17, evaluated using the Heun method with a fixed time step of 2 fs. A zero-temperature damping value of 0.1 was set; however, the equilibrium thermodynamic distributions do not depend on damping factor, nor on the integration time step as we have verified (a small enough time step is required for numerical convergence however, and also very small—less than 0.001—and very large—greater than 0.5—damping values are difficult to accommodate with good numerical precision). Results for the magnetization length distribution, averaged over >50 000 ensembles following an equal number of thermalization iterations, are shown in Figs. 1(a)–1(c). Very good agreement between the MMC and sLLB solutions is obtained (R^2 values >0.99), also in agreement with the expected distribution in Eq. (7) both below and above T_C. A slight discrepancy for sLLB exists close to T_C, reflecting difficulty in accurate numerical evaluation; however, the more accurate MMC result is in excellent agreement with the theoretical distribution even around T_C. The equilibrium magnetization—Eq. (9)—and relative longitudinal susceptibility—Eq. (8)—input functions are shown in Fig. 2, compared with the values obtained by fitting numerically computed distributions, as shown in Fig. 1, with Eq. (7). This shows that the MMC method correctly reproduces the magnetization length probability distribution across the entire simulated temperature range.

Finally, we verify that the transverse distribution in Eq. (6) is reproduced correctly. For this, the angular deviation from mean direction probability distribution is computed. Thus, for each micromagnetic magnetization configuration, the mean direction is obtained, and for each vector in the ensemble, the polar angle θ to this mean direction is found. Using 100 bins for θ, between the minimum and maximum θ values, a histogram is obtained. This is then averaged over >50 000 ensembles. Example results are shown

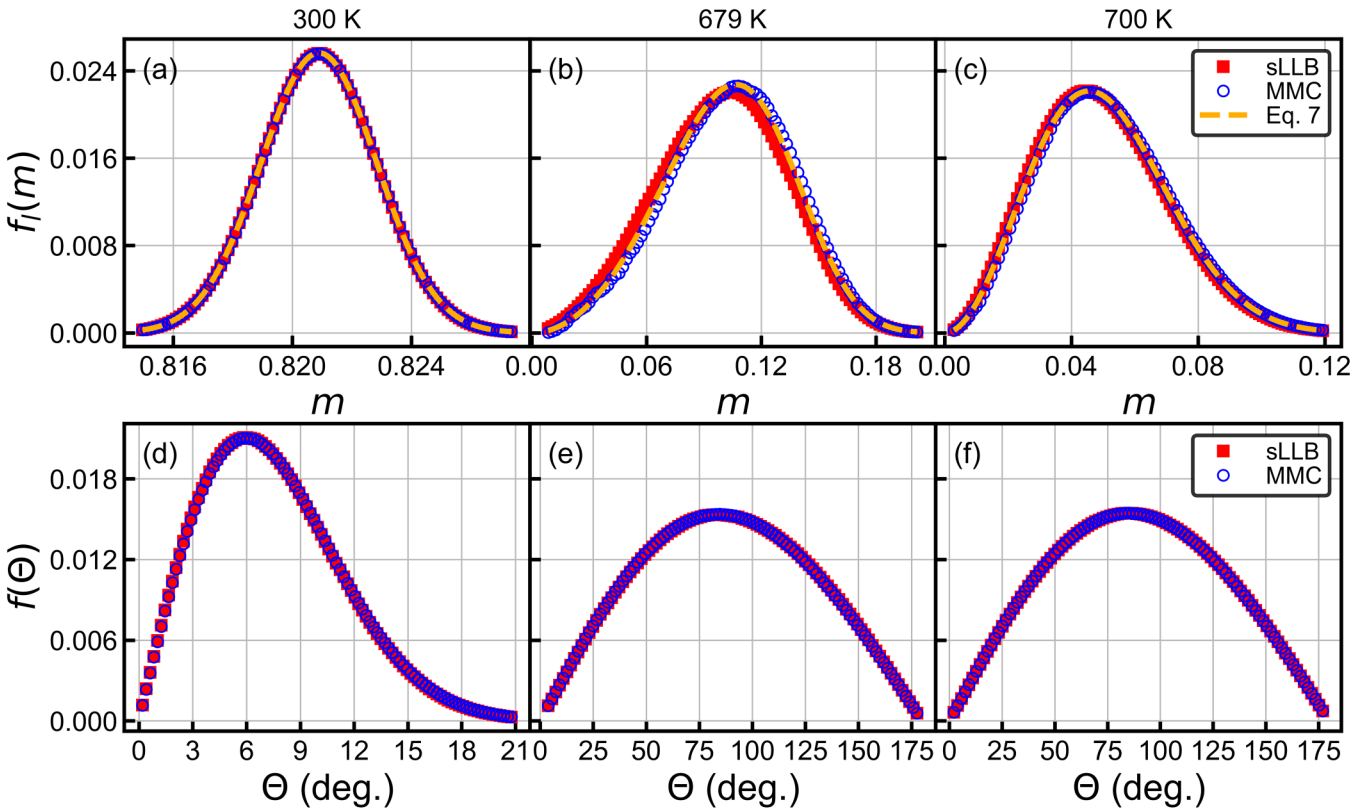

FIG. 1. Verification of single-domain thermodynamic equilibrium properties produced by MMC, compared to sLLB. Examples are shown for 300 K (left panels), 679 K (middle panels), and 700 K (right panels), where $T_C = 680$ K. (a)–(c) Normalized magnetization length probability distributions for indicated temperatures. (d)–(f) Histograms of angular deviation from mean direction, weighted by solid angle unit sphere differential surface area. These are equilibrium distributions averaged over many ensembles (>50 000), which do not depend on damping constant or integration time step in the sLLB equation.

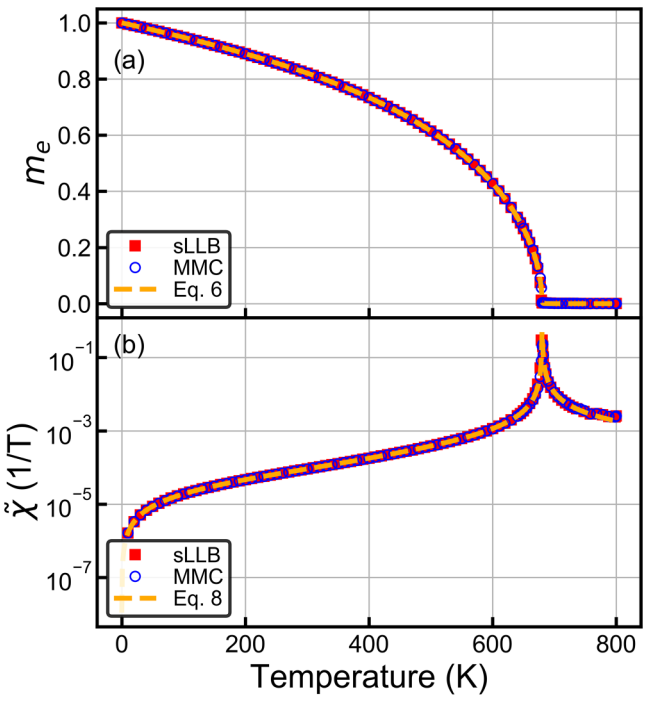

FIG. 2. (a) Normalized equilibrium magnetization length and (b) relative longitudinal susceptibility, computed numerically and compared to model input functions for verification. The distributions produced by MMC and sLLB, respectively, are fitted to obtain to obtain m_e and $\tilde{\chi}$ [with Eq. (7) for the longitudinal distribution].

in Figs. 1(d)–1(f), for both MMC and sLLB, showing excellent agreement. Note the histograms thus obtained are weighted by the bin solid angle differential surface area on the unit sphere; hence, the computed probability tends to zero as θ tends to zero or to π radians.

III. HYSTERESIS LOOP MODELLING

One important application for MMC is finite-temperature hysteresis loop modelling. Here we concentrate on the static hysteresis limit; using kinetic Monte Carlo,[28,29] it is possible to simulate the effect of the field sweep rate. Alternatively TQMC may be employed, and time quantization may also be extended to MMC; however, this is left for a future work. For computation of hysteresis loops, in general, it is essential that the demagnetizing interaction is included, allowing for shape anisotropy effects. Such long-range interactions are notoriously difficult to include in a parallel Monte Carlo algorithm. Since each spin interacts with all other spins, an exact computation of the interaction energy is not compatible with domain decomposition methods. For the atomistic spin lattice case, the dipole–dipole interaction was previously approximately included using a complex stream processing domain decomposition method.[30] Here we discuss a simpler alternative approach, which only requires a single demagnetizing field computation per MMC iteration, and may be achieved using the usual efficient FFT-based convolution method.[17,31] The demagnetizing field may be obtained using the discrete convolution sum shown below, where $\mathbf{N}$ is the demagnetizing tensor,

$$\mathbf{H}_{d,i} = -\sum_j \mathbf{N}_{ij}\mathbf{M}_j,$$
$$F_{d,i} = -V\mu_0 \mathbf{M}_i.\mathbf{H}_{d,i}. \tag{14}$$

The free energy contribution of magnetization vector i is given by $F_{d,i}$, whereas for the exchange interaction the value is compensated for the factor of 1/2 arising from double counting of magnetization vectors in the usual demagnetizing energy density formula. At the start of an MMC iteration, the demagnetizing field is fully computed, and for each trial move, the energy change $\Delta F_{d,i}$ is obtained from Eq. (14) as $\Delta F_{d,i} = -V\mu_0 \Delta\mathbf{M}_i.\mathbf{H}_{d,i}$. Once a trial move is accepted, the demagnetizing field is not immediately updated. Thus, while this approach is also inevitably an approximation, it may be made more accurate by having more than one demagnetizing field update per MMC iteration; for example, since a red–black checkerboard decomposition scheme is used, the demagnetizing field can be updated before each red and black parallel passes. In turn, the red and black passes can be further decomposed to include more demagnetizing field updates. This approach was numerically tested extensively, also against a serial algorithm implementation where $\Delta F_{d,i}$ was computed exactly. Results comparing the parallel and serial MMC implementations are shown in the Appendix B, with no statistical difference found between them. This method works since locally the demagnetizing interaction is relatively weak, and the change in the demagnetizing field from one iteration to another is small. Thus, in thermodynamic equilibrium, locally the trial move acceptance probability is largely driven by the exchange interaction, with $|\Delta F_{\mathrm{ex},i}|$ being over 1–2 orders of magnitude larger than $|\Delta F_{d,i}|$, even for ultrathin films with perpendicular magnetization (see Appendix B). The effect of the demagnetizing field becomes apparent only over many iterations and on a large spatial scale, appearing as a bias in the acceptance probability.

First, we take a simple example to verify that the shape anisotropy effect is correctly reproduced by comparing the MMC method with the sLLB equation solution. Easy and hard axis hysteresis loops in a $400 \times 200 \times 5$ nm $Ni_{80}Fe_{20}$ ellipse, with 5 nm cubic discretization cell size, are computed at 300 and 600 K, with results in Fig. 3 showing excellent agreement. Note that for all the hysteresis loops shown in this work only the increasing field sweep has been simulated, with the decreasing field sweep completed through inverse symmetry. For sLLB, at each field step, the magnetization configuration solution is accepted when the average normalized torque value falls below 10^{-4} (smaller values lead to excessive simulation times). With the MMC method, we need to ensure enough iterations are used to obtain correct thermodynamic equilibrium states. From atomistic Monte Carlo simulations of hysteresis loops, it is known that the switching field estimation becomes increasingly more accurate as the number of Monte Carlo iterations increases.[2] One could run the MMC algorithm with a fixed number of iterations for each field step. Here a more efficient approach is taken; a chunk with a fixed number of iterations (2000) is defined, with an

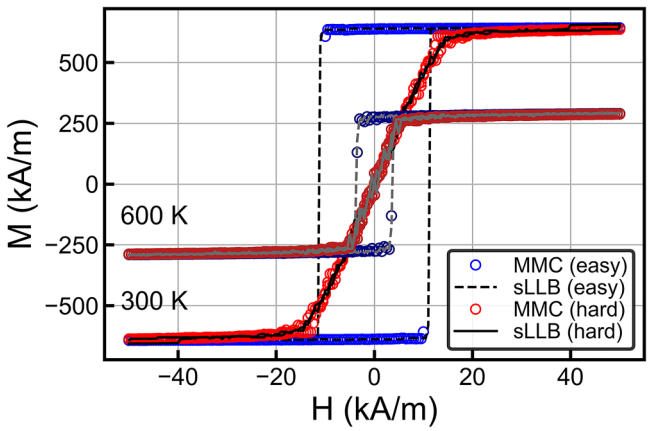

FIG. 3. Hysteresis loops computed in a 400 × 200 × 5 nm $Ni_{80}Fe_{20}$ ellipse at 300 and 600 K, compared between the MMC and sLLB methods, along the easy axis and the in-plane hard axis with 200 field steps. A shape anisotropy arises due to the demagnetizing interaction, with no magnetocrystalline anisotropy included.

ensemble average magnetization value computed for each chunk. For each field step, the MMC algorithm is then executed for at least two chunks of iterations, and if their respective final average magnetization values along the applied field direction are close enough within an acceptance threshold (0.01 normalized change acceptance threshold used), the computation accepts the last chunk average magnetization and proceeds to the next applied field value. This adaptive approach ensures that a small number of iterations are used at parts of the hysteresis loop which change slowly, and a large number of iterations are expended at switching events or at steep parts of the hysteresis curve.

As a further test, we show the hysteresis loops obtained for a $400 \times 200 \times 100$ nm $Ni_{80}Fe_{20}$ ellipsoid at 300 K, also discretized using a 5 nm cubic cell size, computed along the easy, medium, and hard axes. Here MMC is compared with results obtained using the steepest descent (SDesc) energy minimizer,[3] where field steps are considered solved when the maximum normalized torque value falls below 10^{-5}. This is used as a quasi-zero temperature method, where the material parameters are simply rescaled for the required temperature, but otherwise the SDesc method does not include stochasticity or a magnetization length distribution. A very good agreement is observed for the medium and hard axes, with hysteresis loop behavior largely dictated by the shape anisotropy effect. A reasonable agreement is also obtained for the easy axis hysteresis loop; however, here stochasticity also plays a part, resulting in magnetization configuration switching to a vortex state close to the zero field sooner for MMC compared to SDesc; the zero-field vortex state is shown in the inset of Fig. 4(a). In the Appendix A, the easy-axis ellipsoid hysteresis loops are plotted at higher temperatures, showing the SDesc solution becomes increasingly inaccurate as the temperature increases, thus necessitating the use of MMC.

Finally, we test the MMC method by computing the hysteresis loop in a large-scale granular Fe film with cubic anisotropy

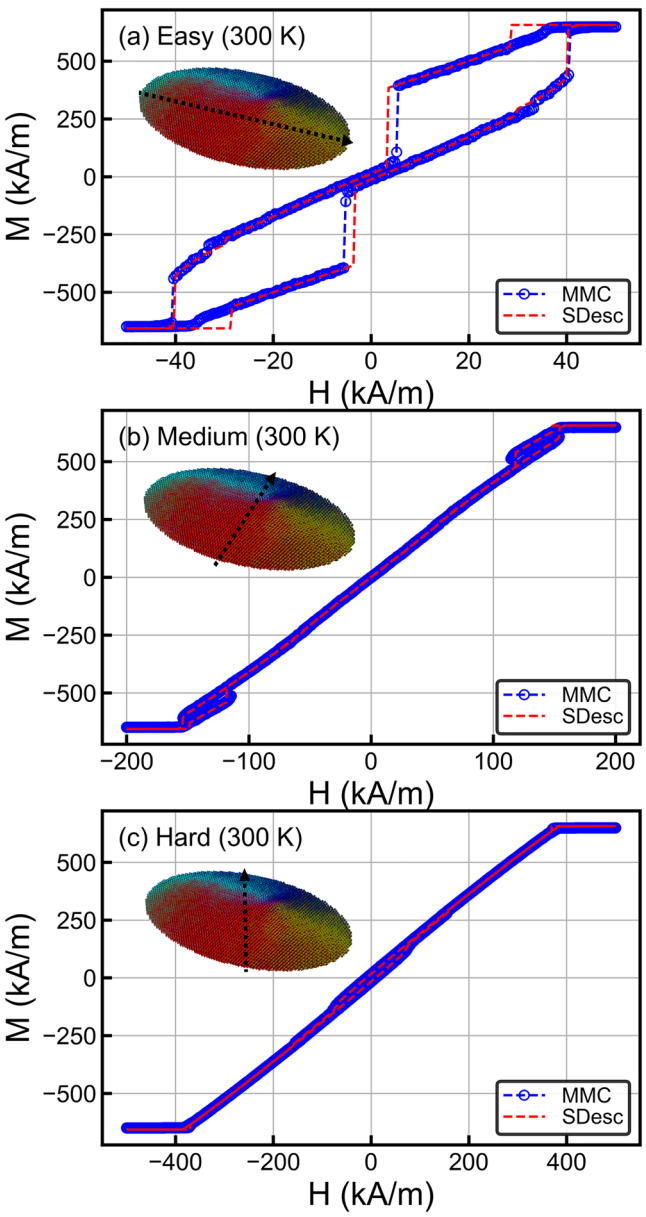

FIG. 4. Hysteresis loops computed in a 400 × 200 × 100 nm $Ni_{80}Fe_{20}$ ellipsoid at 300 K, compared between the MMC and SDesc methods, along the indicated (a) easy, (b) medium, and (c) hard axes. For (a), 250 field steps were used, and for (b) and (c), 1000 field steps were used. The SDesc energy minimization solver is applied with material parameters rescaled for $T = 300$ K but otherwise does not include stochasticity and the magnetization length is constrained to the equilibrium value. The insets show the vortex state obtained at zero field from MMC.

($M_{s0} = 1.71$ MA/m, $A_0 = 21$ pJ/m, $K_1 = 48$ kJ/m^3 fourth order anisotropy constant, $K_2 = -10$ kJ/m^3 sixth order anisotropy constant, and $T_C = 1044$ K). For the anisotropy constants, a $m_e^{l(l+1)/2}$ scaling law[32] is used, with l being the anisotropy term order. The simulation

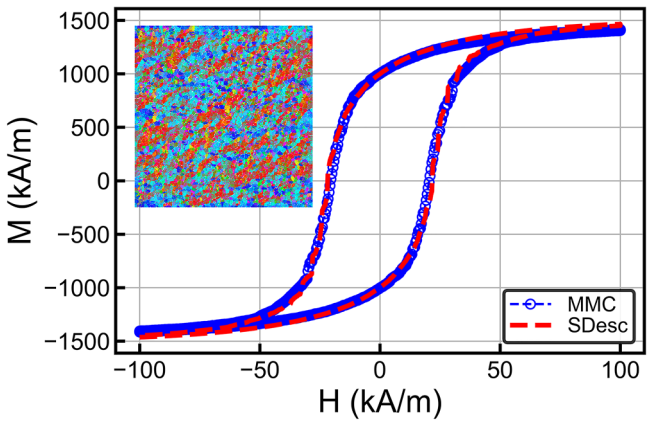

FIG. 5. Hysteresis loop in a cubic anisotropy Fe film with 20 nm thickness and granular structure with 10 nm average grain size. The simulation space contains over 12 000 grains discretized using a 2 nm cubic cell size. The hysteresis loops are computed at 300 K with the MMC and SDesc methods, respectively, using 500 field steps. The inset shows the magnetization configuration obtained from MMC at the coercive field (red denotes grains pointing right and blue pointing left).

space consists of a $800 \times 800 \times 20\ \text{nm}^3$ mesh with periodic boundary conditions in the plane and cubic discretization cell with 2 nm cell size (total of 1.6×10^6 cells included in simulation). The grains are generated using three-dimensional Voronoi tessellation with average 10 nm spacing between seed points and with phase separation (i.e., grains interact through the demagnetizing field only). A typical granular structure generated is shown in the inset of Fig. 5, with the resulting hysteresis loops obtained from MMC and temperature-rescaled SDesc also shown for $T = 300$ K. The field was applied along the in-plane horizontal direction (along cubic easy axis). A good agreement is obtained between the two methods, confirming the demagnetizing interaction is correctly evaluated in the implemented MMC method. Granular films are important for magnetic storage media, including heat-assisted magnetic recording.[33] Specialized methods exist for computing hysteresis loops in granular media, including a thermal activation model[34] and micromagnetic kinetic theory.[35] The MMC approach presented here, however, is a general-purpose method for computing thermodynamic equilibrium states; the resulting collection of states are the same as those that would be obtained by integrating the sLLB equation given sufficient simulation time. For relaxation problems, the MMC method is over 2–3 orders of magnitude faster compared to sLLB. We also note that for the granular film problem of Fig. 5, the MMC method is slightly faster (typical computation time ∼1 h on a modern GPU) than the SDesc method, which requires many iterations to reach the normalized torque convergence threshold of 10^{-5}.

IV. MAGNETIC THIN FILMS WITH DMI

The free energy contribution of the interfacial DMI term is given below, which is included in addition to the direct exchange contribution of Eq. (10),

$$F_{i\text{DMI},i} = -V\frac{2D}{M_e^2}\mathbf{M}_i.(\hat{\mathbf{z}}\nabla.\mathbf{M}_i - \nabla M_{z,i}). \tag{15}$$

Here we simulate the finite-temperature hysteresis loops in thin chiral Co/Pt films ($M_{s0} = 600$ kA/m, $A_0 = 10$ pJ/m, uniaxial anisotropy with perpendicular easy axis and second-order anisotropy constant $K_u = 300\ \text{kJ/m}^3$, and $T_C = 600$ K), where the interfacial DMI is included as $D(T) = D_0 m_e^2$[36] in Eq. (15), with $D_0 = -3\ \text{mJ/m}^2$ being the zero-temperature micromagnetic DMI constant. The simulation space is taken as $1000 \times 1000 \times 2\ \text{nm}^3$ with periodic boundary conditions in the plane and the cubic discretization cell with 2 nm cell size. Hysteresis loops at 300, 350, and 400 K are shown in Fig. 6, where the field is applied perpendicular to the plane. The hysteresis loops are typical of experimental results.[37] A labyrinth domain structure is observed at the zero field in all cases, resulting in sheared hysteresis loops. Inspecting the increasing field sweep, for $T = 300$ K, the labyrinth domain structure is suddenly formed at a negative field, nucleated through thermal activation, as indicated in the inset of Fig. 6(a). As the field strength is increased, the labyrinth domain structure is gradually reduced, eventually forming a small number of skyrmions; further increasing the field results in thermal annihilation of skyrmions, leading to saturation. The magnetization reversal process depends on the sample temperature, not only due to the increased effect of stochasticity, but more importantly due to the temperature dependence of the DMI constant and effective anisotropy. Thus, at higher temperatures, instead of nucleating a labyrinth domain structure, first skyrmions are nucleated, which then grown into a labyrinth structure as shown in Figs. 6(b) and 6(c). Also at higher temperatures, increasing the field toward saturation results in a dense array of skyrmions formed out of the labyrinth structure, approximately arranged into a hexagonal lattice—see inset in Fig. 6(b). The thermodynamic equilibrium states arising at each field step for the hysteresis loops in Fig. 6 are detailed in the Multimedia view (see Fig. 6 caption).

Simulation of such hysteresis loops in chiral films, with rotational symmetry about the applied field axis, is problematic with quasi-zero temperature methods such as SDesc, since the nucleation and annihilation of skyrmions and labyrinth domain structure are principally a thermally activated process. With the SDesc method, generation of a labyrinth domain structure from a uniform state purely by energy minimization requires breaking of rotational symmetry and topological protection and is strongly dependent on numerical floating point errors. Thus, the SDesc hysteresis loop shown in Fig. 6(a) is neither in quantitative nor in qualitative agreement with the MMC simulations, also failing the reproduce the gradual transition from the labyrinth domain structure to skyrmions and gradual thermal annihilation of skyrmions toward saturation; instead, a sudden jump is observed from a near-labyrinth domain structure to saturation.

Finally, we also compute the hysteresis loop with a non-uniform temperature profile, in particular, a Gaussian temperature profile as in Ref. 38, with 300 nm width, reaching a maximum of 400 K at the center, from 300 K at the extremities. Such non-uniform temperature profiles are encountered in ultrafast laser-

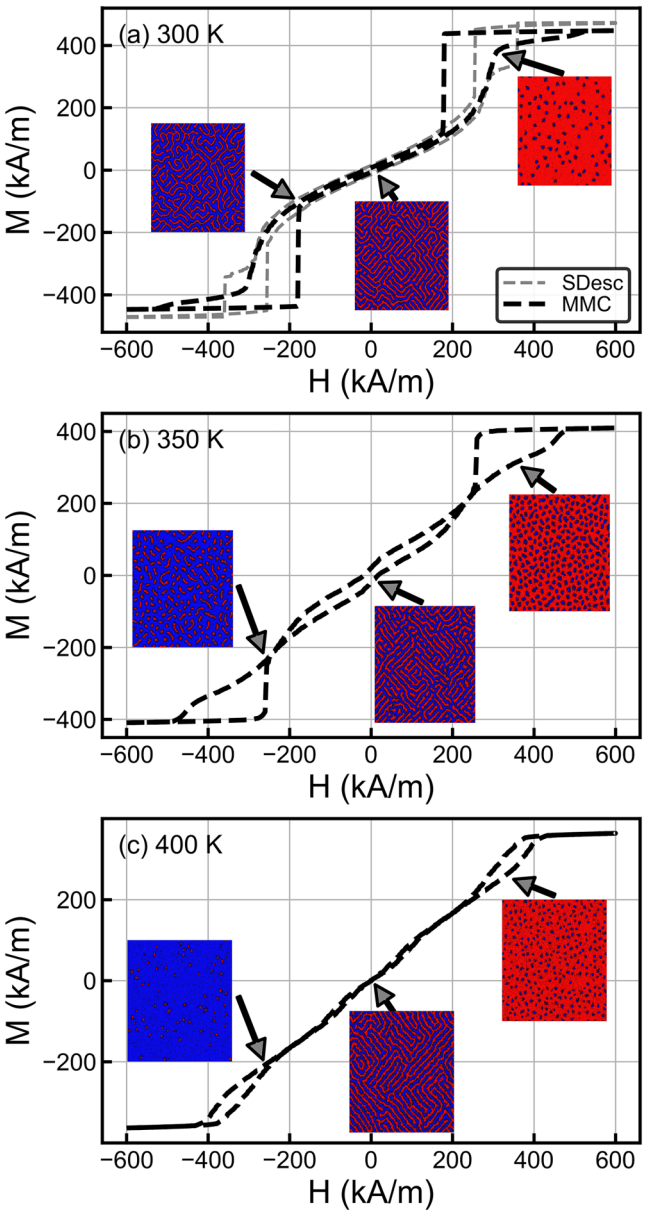

FIG. 6. Hysteresis loops in a thin Co film with interfacial DMI and perpendicular anisotropy, 1000 × 1000 × 2 nm with in-plane periodic boundary conditions, computed for (a) 300, (b) 350, and (c) 400 K using 600 field steps. The insets show the perpendicular magnetization component at the indicated points on the increasing field sweep, with blue denoting magnetization into the plane and red out of the plane. In (a), the SDesc energy minimizer solution is shown for comparison. Multimedia views: https://doi.org/10.1063/5.0059745.1; https://doi.org/10.1063/5.0059745.2; https://doi.org/10.1063/5.0059745.3

induced skyrmion nucleation studies.[37–40] While the MMC method evidently does not reproduce the dynamics, it may be used to analyze the states resulting on a long time-scale, such as mixed labyrinth domain and skyrmion states. Results are shown in Fig. 7. In

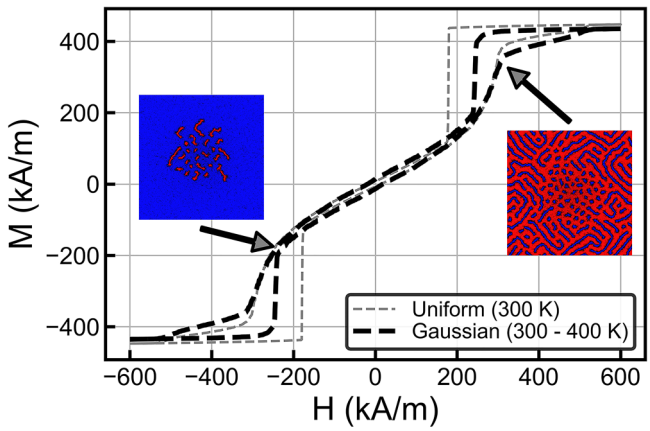

FIG. 7. Hysteresis loop in the same Co film of Fig. 6, using instead a Gaussian temperature profile with 300 nm width, reaching a maximum of 400 K at the center, from 300 K at the extremities. The insets show the perpendicular magnetization component at the indicated points on the increasing field sweep, with blue denoting magnetization into the plane and red out of the plane. Multimedia view: https://doi.org/10.1063/5.0059745.4

contrast to simulation with a uniform temperature, where a labyrinth domain structure is nucleated, instead a number of skyrmions are nucleated inside the Gaussian profile at a larger negative field, which then grows into a labyrinth domain structure. On the positive side of the hysteresis loop, first a number of skyrmions are formed from the labyrinth structure inside the Gaussian profile, resulting in a mixed state as noted in a recent experimental study.[37]

The MMC method may thus be used to study thermodynamic equilibrium states also for materials with DMI, which includes hysteresis loop modelling, but also relaxed states in magnetic nanostructures, for example, as observed in a recent study on Co/Pt multi-layered nano-dots.[41] For such multi-layered structures, the demagnetizing field used for the MMC method may also be computed using the multi-layered convolution algorithm.[31] The analysis of skyrmion arrangements and temperature-driven diffusive motion in magnetic nano-structures was previously done using a quasi-particle Monte Carlo model.[42] The MMC method may also be used for such studies to analyze the probability distribution of skyrmion positions, having the advantage of treating the energy terms on an equal footing with micromagnetic approaches, with full spatial resolution. Thus, in particular, the MMC method naturally takes into account skyrmion deformations, thermal nucleation, and annihilation of skyrmions.

V. ARTIFICIAL SPIN ICES

Artificial spin ices (ASI) is an active and growing field of research; for recent reviews, see Refs. 43 and 44. Here we briefly point out the applicability of the MMC method to the study of ASI. Monte Carlo methods have been successfully applied to the study of ASI, relying on a point dipole approximation for the

magnetic moments of islands comprising ASI arrays.[45,46] On the one hand, this allows computation of the blocking temperature,[47] T_B; annealing with $T > T_B$ (normally $T_B < T_C$) allows the magnetic islands to settle into a different overall energy state, as the energy barriers for flipping their moment directions are overcome, dictated by magnetic frustration due to the dipolar interaction. Use of the dipole approximation Monte Carlo method also allows the study of statistics of the vertex population types (vertex configurations grouped by the energy state). The MMC method presented here may also be used, having the advantage of not relying on a dipole approximation for the magnetic islands moments. This allows, for example, resolving the domain configuration of magnetic islands, which may not be in a single domain state, particularly for larger magnetic islands. Effects due to magnetic islands shape can in principle be taken into account, and also connected ASI arrays may be studied, where the exchange interaction contributes to frustration. Thus, the MMC approach is a more general method compared to the point dipole Monte Carlo approach; the computational complexity is greater; however, efficient use may be made of GPUs, which, as we show below, allows simulations of ASI arrays of dimensions approaching those used in experimental studies.

In Fig. 8, we show results for a square ASI array, with dimensions of $6\,\mu\text{m} \times 6\,\mu\text{m} \times 25$ nm. The $Ni_{80}Fe_{20}$ islands are stadium-shaped and of dimensions $200 \times 40 \times 25$ nm, with lattice spacing of 250 nm. The simulation space was discretized using a 5 nm cubic cell size, with in-plane periodic boundary conditions, thus resulting in 7.2×10^6 simulation cells. An example region of the simulated ASI array is shown in Fig. 8(a). Here we compute the blocking temperature T_B as well as the vertex population statistics—for a square ASI, as is well known, there are four vertex types as given, e.g., in Ref. 48; for brevity, the definitions are not repeated here. The simplest approach to compute T_B is by analyzing field-cooled (FC) and zero-field-cooled (ZFC) curves—see Ref. 47. We also use this method with MMC. Thus, starting from a large temperature near T_C, a small field of 10 kA/m, but large enough to switch the magnetic islands along the field direction, is applied—FC—and the magnetization length in thermodynamic equilibrium along the applied field direction (horizontal direction in Fig. 8) is recorded. The same is repeated in zero field—ZFC—and the temperature differential of the FC and ZFC difference curve is plotted in Fig. 8(c); the point of minimum is the blocking temperature, obtained as $T_B = 656$ K.

Next, an alternative method of computing T_B, which has the advantage of obtaining statistical information on vertex populations, is used. The ASI array is saturated in a large field (100 kA/m) at room temperature, along the horizontal direction, and then relaxed at the zero field; this starting state, showing all the horizontal islands pointing toward the right (red color), is indicated in Fig. 8(a). Next, an annealing temperature is set and thermodynamic equilibrium achieved, before relaxing the ASI array at room temperature again where the vertex types are counted. This is repeated with increasing annealing temperature, and results are shown in Fig. 8(b). Below T_B, the vertex types are exclusively type 2 and type 3, as these are the only possible types with the horizontal islands all pointing in the same direction. Above T_B however, the magnetic moments overcome the energy barrier and settle into a different energy state, giving rise to a significant number of type 1 vertices,

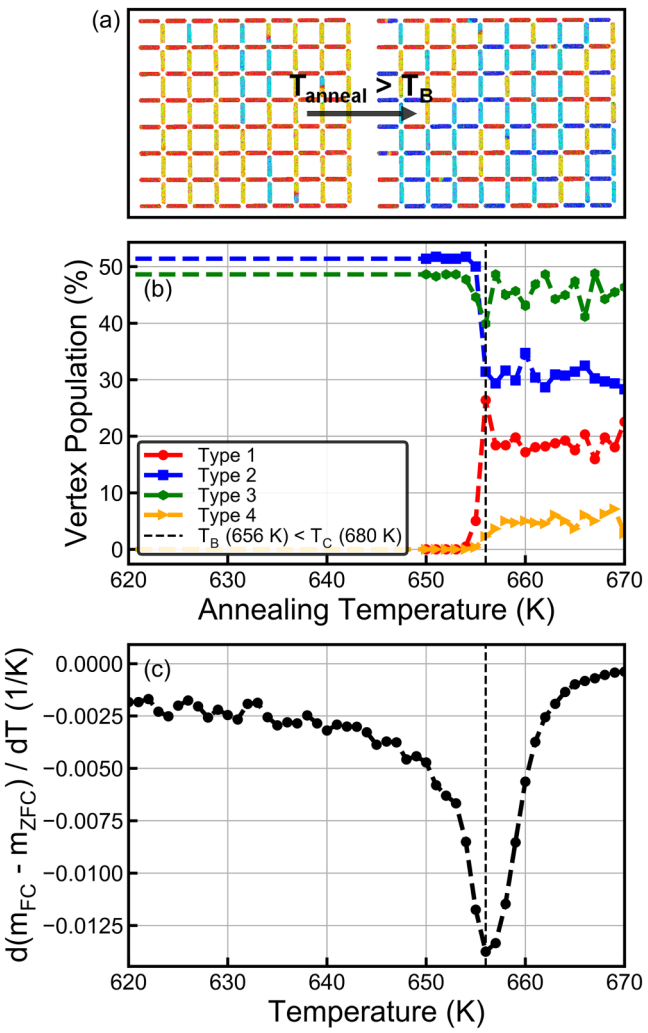

FIG. 8. Computation of blocking temperature T_B and vertex populations in square ASI. The $Ni_{80}Fe_{20}$ islands are stadium-shaped and of dimensions $200 \times 40 \times 25$ nm, with lattice spacing of 250 nm. The simulation space is $6\,\mu\text{m} \times 6\,\mu\text{m} \times 25$ nm using periodic boundary conditions in the plane and cubic cell size of 5 nm. (a) Left-side shows a region of the simulated array before annealing obtained at zero field after saturation. The right-side shows the same array, after annealing with a temperature above T_B; some elements are not in a single domain state. Red is magnetization pointing right, blue pointing left, yellow pointing up, and cyan pointing down. (b) Computation of vertex populations as a function of annealing temperature. The T_B value of 656 K is indicated by the vertical dashed line. (c) Direct computation of T_B using FC and ZFC curves, obtaining the same blocking temperature of 656 K as in panel (b).

largely at the cost of type 2 vertices, although a small number of higher energy type 4 vertices are also created. This transition is fairly abrupt at 656 K, in perfect agreement with the FC method shown in Fig. 8(c). It is interesting to note that with these dimensions not all islands are in a single domain state, as seen in Fig. 8(a), with a small number containing a transverse domain wall,

which is stable against thermal fluctuations. Thus, the MMC method may also be used to study ASI, including not only square arrays, but also kagome lattices[49] and magnetic quasicrystals.[50]

VI. CONCLUSIONS

In this work, an efficient method for computing thermodynamic equilibrium states at the micromagnetic length scale was introduced, which mirrors the Metropolis Monte Carlo method commonly used for atomistic spin lattice simulations. Since micromagnetic magnetization vectors are thermodynamic averages of atomistic spins, a magnetization length distribution arises on the micromagnetic length scale. This follows a Maxwell–Boltzmann type distribution, and the micromagnetic Monte Carlo method reproduces this, in agreement with the stochastic Landau–Lifshitz–Bloch equation, by use of an additional magnetization length change trial move. Thus, the micromagnetic Monte Carlo method gives rise to the same collection of magnetization vector ensembles in thermodynamic equilibrium as the dynamic stochastic Landau–Lifshitz–Bloch equation does given sufficient simulation time. This approach is far more efficient however, allowing computation of relaxed states in large-scale systems, for which the use of the dynamic approach is not practically feasible. Particular examples have been given, including computation of hysteresis loops, both in two-dimensional and in three-dimensional structures, granular films, chiral magnetic films, and study of artificial spin ices. The set of applications is not limited to these cases however, as the micromagnetic Monte Carlo method is a general approach for computing relaxed states at finite temperatures, and further work is required to fully exploit the range of applicability. Possible future extensions include the use of time quantization to allow study of, for example, the field sweep rate on hysteresis loops and grain reversal times. Finally, the method introduced here was applied to ferromagnetic materials; however, a future work will investigate extensions to two-sublattice models, allowing applications to ferrimagnetic and antiferromagnetic materials.[51]

APPENDIX A: COMPARISON OF MMC AND QUASI-ZERO TEMPERATURE SOLUTIONS AT HIGH TEMPERATURES AND FIELDS

The SDesc and MMC methods generally agree well at low temperatures far below T_C, especially when magnetization reversal occurs largely through coherent rotation. An important exception to this is for processes where magnetization reversal is principally driven by thermally activated reversal, and we have given an example in the main text for chiral magnetic thin films. For such problems, quasi-zero temperature methods (SDesc) are inadequate. Here we further show also for high temperatures the SDesc method is increasingly inaccurate, necessitating the use of MMC.

Figure 9 shows the $Ni_{80}Fe_{20}$ ellipsoid problem of Fig. 4, with hysteresis loops given along the easy axis for 300, 500, 600, and 650 K ($T_C = 680$ K). As the temperature increases, the MMC and SDesc solutions increasingly diverge. The difference between the solutions at high fields is due to lack of stochasticity in the SDesc method, which becomes increasingly important at higher temperatures, as the average angular deviation from the mean direction

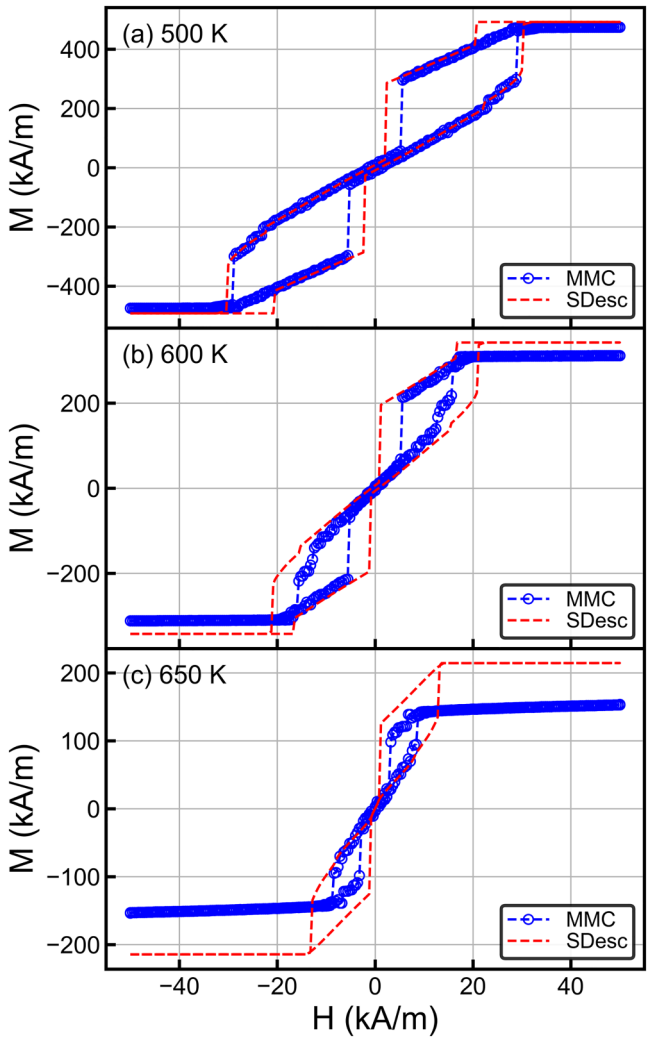

FIG. 9. Comparison of MMC and SDesc methods for the ellipsoid problem of Fig. 4, showing the easy axis hysteresis loops at higher temperatures for (a) 500, (b) 600, and (c) 650 K. As the temperature increases, the SDesc solution becomes increasingly inaccurate due to lack of stochasticity and uniform magnetization length.

increases [see Figs. 1(d)–1(f)]. Thus, the SDesc solutions reach the magnetization saturation value at low fields, failing to reproduce a realistic high field behavior—comparisons of high field behavior for the SDesc and MMC solutions are shown in Fig. 10. For the MMC solutions however, large fields are required at high temperatures to fully saturate the magnetization along the applied field direction, requiring narrowing of the angular deviation from the mean direction probability distribution. It should be noted for the sLLB equation form of Ref. 7—for which the current MMC method reproduces the same thermodynamic equilibrium properties—the un-weighted average magnetization does not coincide with the equilibrium magnetization, as noted in Ref. 7 and as may

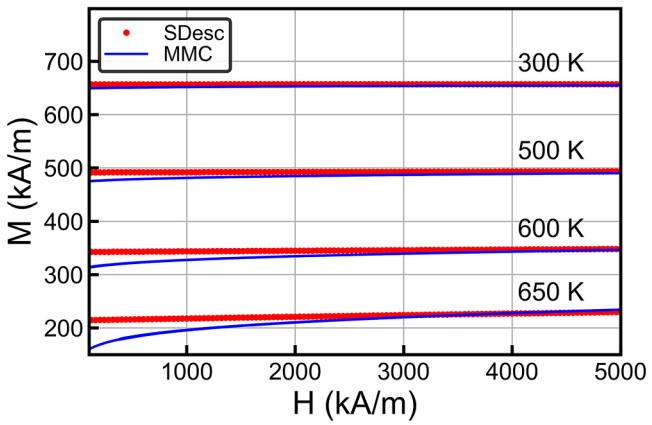

FIG. 10. High-field behavior of easy-axis hysteresis loops for the ellipsoid problem of Figs. 4 and 9.

easily be verified numerically. Conceptually this is problematic, since in atomistic modelling, the two values are identical. This problem has been addressed recently,[52] with an alternative form of the sLLB equation obtained from the LLB equation in Ref. 5. It may be possible to extend the MMC method to this alternative sLLB formulation; however, this is left for future work.

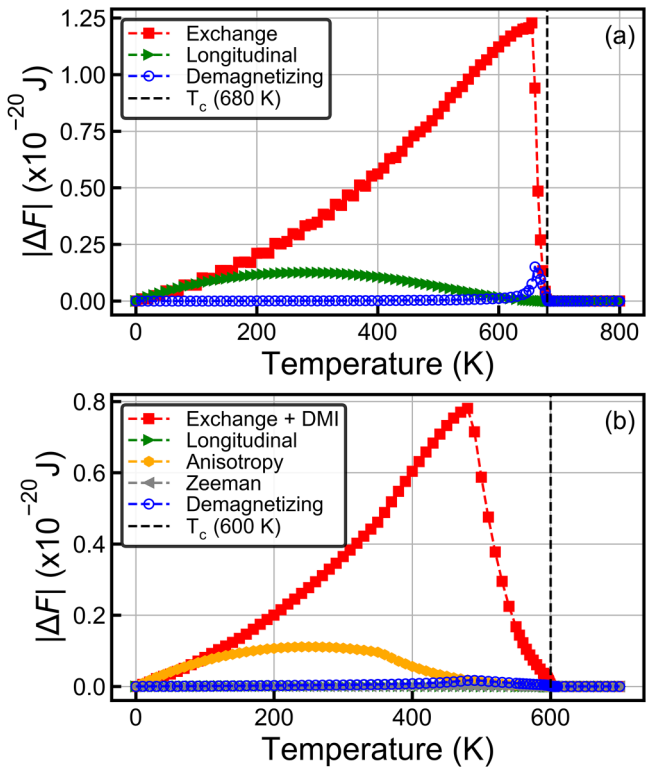

FIG. 11. Average change in free energies for MMC trial moves for (a) the $Ni_{80}Fe_{20}$ ellipsoid problem of Fig. 4, initialized at zero field with the vortex state shown in the insets of Figs. 4 and 4(b) the ultrathin Co/Pt film (here 1 nm Co thickness) of Fig. 6.

APPENDIX B: FREE ENERGY CONTRIBUTIONS TO MMC TRIAL MOVES

The free energy contributions to MMC trial moves are computed (a) for the $Ni_{80}Fe_{20}$ ellipsoid problem of Figs. 4 and 4(b) for the ultrathin Co/Pt film (here 1 nm Co thickness) of Fig. 6, in order to illustrate the relative importance of the different interactions to the trial move acceptance rate. Results are shown in Fig. 11 as a function of temperature, with (a) the ellipsoid initialized at zero field with the vortex state shown in the insets to Figs. 4 and 4(b) the ultrathin Co film perpendicularly magnetized and with a 100 kA/m perpendicular magnetic field. The exchange interaction is the dominant contribution, with the demagnetizing interaction typically relatively negligible except when close to T_C. The exchange interaction term is computed using Eq. (10), the demagnetizing interaction term is computed using Eq. (14), and the longitudinal

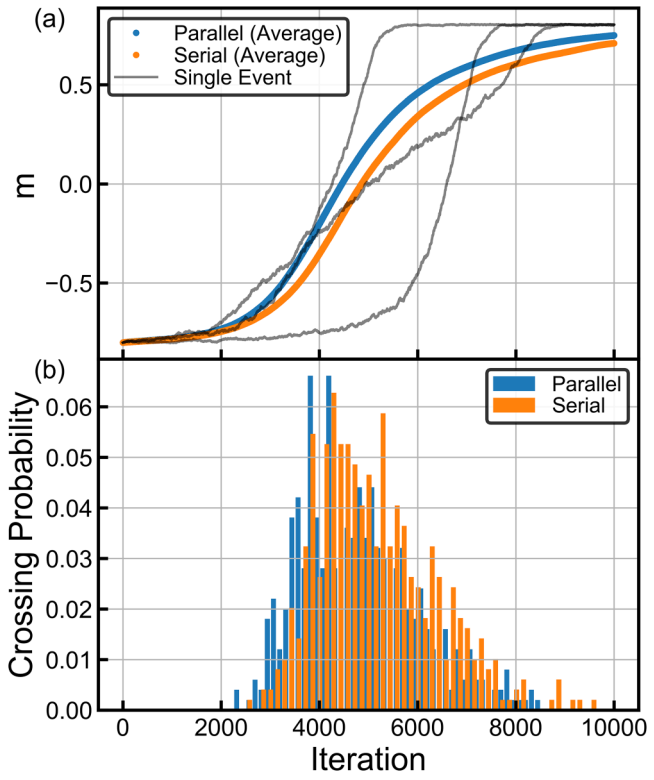

FIG. 12. Magnetization switching for the ellipse problem around the coercive field, H = 12 kA/m, as a function of number of iterations. (a) Averages over 500 switching events, showing normalized magnetization as a function of iteration number, computed with the parallel MMC algorithm, as well as the serial MMC algorithm where the demagnetizing field is updated after every accepted move. Some individual switching events are also shown. (b) Probability of crossing the x axis as a function of number of iterations, shown for both the parallel and serial MMC algorithms.

term is obtained from the energy term appearing in the exponent of Eq. (7). This justifies the use of a single demagnetizing field update per MMC iteration, as consecutive MMC ensembles are largely correlated through the exchange interaction, with the influence of the demagnetizing interaction on thermodynamic equilibrium states being important only after many iterations (typically 10^2–10^4).

Finally, we compare the parallel MMC algorithm, where the demagnetizing field is update once per iteration, with the serial MMC version where the demagnetizing field is updated after every accepted move. The latter thus exactly takes into account the long-range demagnetizing interaction. Magnetization switching events are computed as a function of number of iterations for the ellipse problem of Fig. 3. Starting from the remanence state with magnetization pointing along the $-x$ direction, the coercive field value of $H = 12$ kA/m is applied, and the magnetization along the field recorded over 10 000 iterations. Individual switching events are shown in Fig. 12(a), as well as averages over 500 switching events for both algorithms. The switching probability is strongly influenced by the demagnetizing field, which gives rise to an effective uniaxial anisotropy. The probability of crossing the x axis is plotted in Fig. 12(b) as a function of iteration number. These results show there is no significant difference between the two approaches, again justifying the use of Eq. (14) for including the demagnetizing interaction in the parallel MMC algorithm.

APPENDIX C: MMC AND SLLB COMPUTATION TIMES COMPARISON

Comparisons of computation times between the MMC and sLLB methods are shown here. These are given in Table I for the ellipse and ellipsoid problems of Fig. 3 and 4, respectively. For the ellipse problem, the computations were done on the central processing unit (CPU) using a Linux OS (Ubuntu)—AMD R7 3700X (16 logical cores). For the ellipsoid problem, the computations were done on the GPU—Nvidia GTX 980 Ti.

For sLLB, the RK4 method was used with a fixed time step of 50 fs and a damping value of $\alpha = 0.1$. For non-stochastic equations, higher damping values result in faster relaxation, with an optimum damping value of $\alpha = 1.0$ due to a maximum in the damping torque [proportional to $\alpha/(1+\alpha^2)$]. For sLLB, however, higher damping values require smaller time steps for integration, while smaller damping values result in excessive oscillations, resulting in increased computation times when relaxing; the value $\alpha = 0.1$ is a good compromise. The integration time step was determined by computing the magnetization length probability distribution as shown in Fig. 1. The value of 50 fs is the largest time step that reproduces Eq. (7), with larger time steps resulting in significant deviations from the analytical result before any numerical divergence is observed.

For MMC, the demagnetizing field is computed once per iteration as explained in the main text. For sLLB with the RK4 method, which consists of four sub-steps per time step iteration, normally the demagnetizing field is computed once per sub-step. In order to improve the computation time, a recently proposed method of speeding up explicit evaluation methods using demagnetizing field polynomial extrapolation[53] was used, thus also employing one demagnetizing field evaluation per iteration. As expected, computation times for MMC are significantly smaller, with speedup factors of almost 20 obtained as shown in Table I.

TABLE I. Comparison of computation times between MMC and sLLB for hysteresis loops of ellipse (Fig. 3) and ellipsoid (Fig. 4) problems. These are computed on the CPU, respectively, GPU as indicated, with speedup factor defined as time for sLLB divided by time for MMC computation completion.

Problem	MMC	sLLB	Speedup
Ellipse (Fig. 3)—CPU	107 s	1879 s	17.6
Ellipsoid (Fig. 4)—GPU	747 s	14 342 s	19.2

DATA AVAILABILITY

The data that support the findings of this study are available from the corresponding author upon reasonable request, and the micromagnetic Monte Carlo algorithm code is available at https://github.com/SerbanL/Boris2, Ref. 18.

REFERENCES

[1]N. Metropolis, A. W. Rosenbluth, M. N. Rosenbluth, A. H. Teller, and E. Teller, "Equation of state calculations by fast computing machines," J. Chem. Phys. **21**, 1087 (1953).
[2]Z. Nehme, Y. Labaye, R. Sayed Hassan, N. Yaacoub, and J. M. Greneche, "Modeling of hysteresis loops by Monte Carlo simulation," AIP Adv. **5**, 127124 (2015).
[3]L. Exl, S. Bance, F. Reichel, T. Schrefl, H. Peter Stimming, and N. J. Mauser, "Labonte's method revisited: An effective steepest descent method for micromagnetic energy minimization," J. Appl. Phys. **115**, 17D118 (2014).
[4]W. F. Brown, "Relaxational behavior of fine magnetic particles," J. Appl. Phys. **30**, S130 (1959).
[5]D. A. Garanin, "Fokker–Planck and Landau–Lifshitz–Bloch equations for classical ferromagnets," Phys. Rev. B **55**, 3050 (1997).
[6]D. A. Garanin and O. Chubykalo-Fesenko, "Thermal fluctuations and longitudinal relaxation of single-domain magnetic particles at elevated temperatures," Phys. Rev. B **70**, 212409 (2004).
[7]R. F. L. Evans, D. Hinzke, U. Atxitia, U. Nowak, R. W. Chantrell, and O. Chubykalo-Fesenko, "Stochastic form of the Landau-Lifshitz-Bloch equation," Phys. Rev. B **85**, 014433 (2012).
[8]K. Vahaplar, A. M. Kalashnikova, A. V. Kimel, D. Hinzke, U. Nowak, R. Chantrell, A. Tsukamoto, A. Itoh, A. Kirilyuk, and T. Rasing, "Ultrafast path for optical magnetization reversal via a strongly nonequilibrium state," Phys. Rev. Lett. **103**, 117201 (2009).
[9]N. Kazantseva, D. Hinzke, R. W. Chantrell, and U. Nowak, "Linear and elliptical magnetization reversal close to the Curie temperature," Europhys. Lett. **86**, 27006 (2009).
[10]K. Fukuma and D. J. Dunlop, "Monte Carlo simulation of two-dimensional domain structures in magnetite," J. Geophys. Res. **102**, 5135–5143, https://doi.org/10.1029/96JB03663 (1997).
[11]J. M. González, R. Ramírez, R. Smirnov-Rueda, and J. González, "On the relaxation of simple magnetic systems," J. Appl. Phys. **79**, 6479 (1996).
[12]G. Suran, J. I. Arnaudas, M. Ciria, C. de la Fuente, M. Rivoire, O. A. Chubykalo, and J. M. González, "Evidences of non-Arrhenius magnetic relaxation in macroscopic systems: Experiments and related simulations," Europhys. Lett. **41**, 671–676 (1998).
[13]A. Chrobak, G. Ziółkowski, D. Chrobak, and G. Chełkowska, "From atomic level to large-scale Monte Carlo magnetic simulations," Materials **13**, 3696 (2020).

[14]P. M. Derlet, "Landau–Heisenberg Hamiltonian model for FeRh," Phys. Rev. B **85**, 174431 (2012).
[15]D. Wei, J. Song, and C. Liu, "Micromagnetics at finite temperature," IEEE Trans. Mag. **52**, 7100808 (2016).
[16]S. Duane, A. D. Kennedy, B. J. Pendleton, and D. Roweth, "Hybrid Monte Carlo," Phys. Lett. B **195**, 216–222 (1987).
[17]S. Lepadatu, "Boris computational spintronics—High performance multi-mesh magnetic and spin transport modeling software," J. Appl. Phys. **128**, 243902 (2020).
[18]See https://github.com/SerbanL/Boris2 for source code repository; accessed 9 June 2021.
[19]I. Dzyaloshinsky, "A thermodynamic theory of 'weak' ferromagnetism of antiferromagnetics," J. Phys. Chem. Solids **4**, 241–255 (1958).
[20]T. Moriya, "Anisotropic superexchange interaction and weak ferromagnetism," Phys. Rev. **120**, 91 (1960).
[21]T. Preis, P. Virnau, W. Paul, and J. J. Schneider, "GPU accelerated Monte Carlo simulation of the 2D and 3D Ising model," J. Comput. Phys. **228**, 4468–4477 (2009).
[22]S. Lepadatu, G. McKenzie, T. Mercer, C. R. MacKinnon, and P. R. Bissell, "Computation of magnetization, exchange stiffness, anisotropy, and susceptibilities in large-scale systems using GPU-accelerated atomistic parallel Monte Carlo algorithms," J. Magn. Magn. Mater. **540**, 168460 (2021).
[23]U. Nowak, R. W. Chantrell, and E. C. Kennedy, "Monte Carlo simulation with time step quantification in terms of Langevin dynamics," Phys. Rev. Lett. **84**, 163 (2000).
[24]X. Z. Cheng, M. B. A. Jalil, H. K. Lee, and Y. Okabe, "Mapping the Monte Carlo scheme to Langevin dynamics: A Fokker–Planck approach," Phys. Rev. Lett. **96**, 067208 (2006).
[25]P. V. Melenev, Y. L. Raikher, V. V. Rusakov, and R. Perzynski, "Time quantification for Monte Carlo modelling of superparamagnetic relaxation," Phys. Rev. B **86**, 104423 (2012).
[26]O. Chubykalo, U. Nowak, R. Smirnov-Rueda, M. A. Wongsam, R. W. Chantrell, and J. M. Gonzalez, "Monte Carlo technique with a quantified time step: Application to the motion of magnetic moments," Phys. Rev. B **67**, 064422 (2003).
[27]U. Atxitia, D. Hinzke, O. Chubykalo-Fesenko, U. Nowak, H. Kachkachi, O. N. Mryasov, R. F. Evans, and R. W. Chantrell, "Multiscale modeling of magnetic materials: Temperature dependence of the exchange stiffness," Phys. Rev. B **82**, 134440 (2010).
[28]T. J. Fal, J. I. Mercer, M. D. Leblanc, J. P. Whitehead, M. L. Plumer, and J. van Ek, "Kinetic Monte carlo approach to modeling thermal decay in perpendicular recording media," Phys. Rev. B **87**, 064405 (2013).
[29]T. J. Fal, M. L. Plumer, J. P. Whitehead, J. I. Mercer, J. van Ek, and K. Srinivasan, "Simulations of magnetic hysteresis loops for dual layer recording media," Appl. Phys. Lett. **102**, 202404 (2013).
[30]M. C. Ambrose and R. L. Stamps, "Monte Carlo simulation of the effects of higher-order anisotropy on the spin reorientation transition in the two-dimensional Heisenberg model with long-range interactions," Phys. Rev. B **87**, 184417 (2013).
[31]S. Lepadatu, "Efficient computation of demagnetizing fields for magnetic multilayers using multilayered convolution," J. Appl. Phys. **126**, 103903 (2019).
[32]H. B. Callen and E. Callen, "The present status of the temperature dependence of magnetocrystalline anisotropy, and the l(l+1)/2 power law," J. Phys. Chem. Solids **27**, 1271 (1966).
[33]D. Weller, G. Parker, O. Mosendz, A. Lyberatos, D. Mitin, N. Y. Safonova, and M. Albrecht, "Review article: FePt heat assisted magnetic recording media," J. Vac. Sci. Technol. B **34**, 060801 (2016).
[34]J. Xue and R. H. Victora, "Micromagnetic predictions for thermally assisted reversal over long time scales," Appl. Phys. Lett. **77**, 3432 (2000).
[35]G. J. Parker and W. N. G. Hitchon, "A kinetic theory of micromagnetic time evolution," Phys. Lett. A **377**, 2388–2392 (2013).
[36]L. Rózsa, U. Atxitia, and U. Nowak, "Temperature scaling of the Dzyaloshinsky-Moriya interaction in the spin wave spectrum," Phys. Rev. B **96**, 094436 (2017).
[37]K. Gerlinger, B. Pfau, F. Büttner, M. Schneider, L.-M. Kern, J. Fuchs, D. Engel, C. M. Günther, M. Huang, I. Lemesh *et al.*, "Application concepts for ultrafast laser-induced skyrmion creation and annihilation," Appl. Phys. Lett. **118**, 192403 (2021).
[38]S. Lepadatu, "Emergence of transient domain wall skyrmions after ultrafast demagnetization," Phys. Rev. B **102**, 094402 (2020).
[39]S.-G. Je, P. Vallobra, T. Srivastava, J.-C. Rojas-Sánchez, T. H. Pham, M. Hehn, G. Malinowski, C. Baraduc, S. Auffret, G. Gaudin *et al.*, "Creation of magnetic skyrmion bubble lattices by ultrafast laser in ultrathin films," Nano Lett. **18**, 7362 (2018).
[40]N. Novakovic-Marinkovic, M.-A. Mawass, O. Volkov, P. Makushko, W. Dieter Engel, D. Makarov, and F. Kronast, "From stripes to bubbles: Deterministic transformation of magnetic domain patterns in Co/Pt multilayers induced by laser helicity," Phys. Rev. B **102**, 174412 (2020).
[41]I. V. Vetrova, M. Zelent, J. Šoltýs, V. A. Gubanov, A. V. Sadovnikov, T. Ščepka, J. Dérer, R. Stoklas, V. Cambel, and M. Mruczkiewicz, "Investigation of self-nucleated skyrmion states in the ferromagnetic/nonmagnetic multilayer dot," Appl. Phys. Lett. **118**, 212409 (2021).
[42]A. F. Schäffer, L. Rózsa, J. Berakdar, E. Y. Vedmedenko, and R. Wiesendanger, "Stochastic dynamics and pattern formation of geometrically confined skyrmions," Commun. Phys. **2**, 72 (2019).
[43]S. H. Skjærvø, C. H. Marrows, R. L. Stamps, and L. J. Heyderman, "Advances in artificial spin ice," Nat. Rev. Phys. **2**, 13–28 (2020).
[44]P. Schiffer and C. Nisoli, "Artificial spin ice: Paths forward," Appl. Phys. Lett. **118**, 110501 (2021).
[45]Z. Budrikis, K. L. Livesey, J. P. Morgan, J. Akerman, A. Stein, S. Langridge, C. H. Marrows, and R. L. Stamps, "Domain dynamics and fluctuations in artificial square ice at finite temperatures," New J. Phys. **14**, 035014 (2012).
[46]J. M. Porro, S. A. Morley, D. A. Venero, R. Macêdo, M. C. Rosamond, E. H. Linfield, R. L. Stamps, C. H. Marrows, and S. Langridge, "Magnetization dynamics of weakly interacting sub-100 nm square artifcial spin ices," Sci. Rep. **9**, 19967 (2019).
[47]D. Serantes, D. Baldomir, M. Pereiro, J. Rivas, C. Vázquez-Vázquez, M. C. Buján-Núñez, and J. E. Arias, "Magnetic field-dependence study of the magnetocaloric properties of a superparamagnetic nanoparticle system: A Monte Carlo simulation," Phys. Status Solidi A **205**, 1349–1353 (2008).
[48]R. F. Wang, C. Nisoli, R. S. Freitas, J. Li, W. McConville, B. J. Cooley, M. S. Lund, N. Samarth, C. Leighton, V. H. Crespi, and P. Schiffer, "Artificial 'spin ice' in a geometrically frustrated lattice of nanoscale ferromagnetic islands," Nature **439**, 303–306 (2006).
[49]Y. Qi, T. Brintlinger, and J. Cumings, "Direct observation of the ice rule in an artificial kagome spin ice," Phys. Rev. B **77**, 094418 (2008).
[50]D. Shi, Z. Budrikis, A. Stein, S. A. Morley, P. D. Olmsted, G. Burnell, and C. H. Marrows, "Frustration and thermalization in an artificial magnetic quasicrystal," Nat. Phys. **14**, 309–314 (2018).
[51]J. Barker and U. Atxitia, "A review of modelling in ferrimagnetic spintronics," J. Phys. Soc. Jpn. **90**, 081001 (2021).
[52]M. Menarini and V. Lomakin, "Thermal fluctuations in the Landau–Lifshitz–Bloch model," Phys. Rev. B **102**, 024428 (2020).
[53]S. Lepadatu, "Speeding up explicit numerical evaluation methods for micromagnetic simulations using demagnetizing field polynomial extrapolation," arXiv:2107.06729v1 (2021).